

# A detailed 3D finite element analysis of the peeling behavior of a gecko spatula

Roger A. Sauer <sup>1</sup>

*Aachen Institute for Advanced Study in Computational Engineering Science (AICES), RWTH Aachen University, Templergraben 55, 52056 Aachen, Germany,*

Matthias Holl <sup>2</sup>

*Institute of Continuum Mechanics, Leibniz University Hanover, Appelstr. 11, 30167 Hanover, Germany*

Published<sup>3</sup> in *Computer Methods in Biomechanics and Biomedical Engineering*,

DOI: [10.1080/10255842.2011.628944](https://doi.org/10.1080/10255842.2011.628944)

Submitted on 28 January 2011, Revised on 5 August 2011, Accepted on 29 September 2011

---

## Abstract

This paper presents a detailed finite element analysis of the adhesion of a gecko spatula. The gecko spatulae form the tips of the gecko foot hairs that transfer the adhesional and frictional forces between substrate and foot. The analysis is based on a parameterized description of the three-dimensional geometry of the spatula, that only requires 12 parameters. The adhesion is described by a non-linear computational contact formulation that accounts for the van der Waals interaction between spatula and substrate. The spatula adhesion model is implemented using an enriched contact finite element formulation recently developed by the first author. The finite element model is then used to simulate the peeling behavior of the gecko spatula under applied vertical and rotational loading for various model parameters. Considered are variations of the material stiffness, adhesional strength and range, stiction, spatula size and spatula inclination, to account for the natural variation of spatula properties. The study demonstrates that the spatula can function over a wide range of conditions. The computed pull-off forces are in agreement with experimental results reported in the literature. The study also examines the energy required for the spatula pull-off. The proposed model is ideal to study the influence of substrate roughness on the spatula adhesion, as is finally demonstrated.

**Keywords:** gecko adhesion, van der Waals interaction, computational contact mechanics, non-linear finite element methods, peeling

---

## 1 Introduction

The tokay gecko has developed a remarkable adhesion mechanism that has fascinated and inspired people for many years. The toes of the gecko are covered with hundreds of thousands of micrometer-fine hairs that each branch into hundreds of finer hairs, the so-called spatulae. The spatulae transfer the adhesive and frictional forces between gecko and substrate, and, due to their high flexibility, thereby undergo very large mechanical deformations and rotations. The spatulae thus form an elemental part in the understanding of gecko adhesion. Many models

---

<sup>1</sup>corresponding author, email: [sauer@aices.rwth-aachen.de](mailto:sauer@aices.rwth-aachen.de), phone: +49 241 80 99129, fax: +49 241 80 628498

<sup>2</sup>graduate student, email: [holl@ikm.uni-hannover.de](mailto:holl@ikm.uni-hannover.de)

<sup>3</sup>This pdf is the personal version of an article whose final publication is available at [www.tandfonline.com](http://www.tandfonline.com)

have been proposed in the literature to describe the adhesion mechanism of the gecko (Kwaki and Kim, 2010; Sauer, 2009). But up to now no detailed 3D mechanical model has been considered to study the behavior of the spatula. To the best of our knowledge, this is the first such analysis reported in the literature. Due to the non-linearities of large deformations a computational approach is required. The two major challenges in formulating such a computational spatula model are the spatula geometry and the adhesion mechanism itself (Sauer, 2010). In the present paper a detailed but relatively simple 3D parametric model is constructed that describes the spatula geometry such that shape variations can be accommodated easily. This new model is a considerable advancement of the structural beam model developed in Sauer (2009). The spatula geometry is discretized into 3D finite elements using a standard non-linear continuum formulations to describe the structure and using the contact formulation of Sauer and Li (2007), Sauer and Wriggers (2009) and Sauer (2011a) to describe the adhesion between pad and substrate. The proposed model is ideal to study in detail the adhesive contact behavior of the spatula, like its peeling and detachment behavior, and thereby analyze the stress and deformation of the structure. Due to the generality of the contact formulation, the model can also be used to study spatula adhesion on rough surfaces. In this paper, the spatula model is used to study the pull-off behavior for different model parameters that account for variations in spatula size, spatula stiffness, strength of adhesion, range of adhesion, surface roughness, stiction and loading conditions. Such a study is particularly useful since the natural spatula properties are subject to variation.

The remainder of this paper is structured as follows: Sec. 2 presents the geometric model for the gecko spatula and discusses its model parameters. The computational contact model used to describe the adhesion between spatula and substrate is then addressed in Sec. 3. Sec. 4 considers and analyzes several numerical examples that demonstrate the capabilities of the model and allow to draw several conclusions on the spatula behavior. The presentation is summarized in Sec. 5.

## 2 Modeling the spatula geometry

This section proposes a relatively simple, but detailed 3D model which aims at describing the spatula geometry realistically and which is then used in the simulations presented in Sec. 4. The spatula description is based on a parameterized model, so that certain geometrical changes can be incorporated automatically.

The gecko spatula is a very small, elongated structure, consisting of a very thin flat pad attached to a cylindrical shaft as is shown in Fig. 1.a. This microscope image is adopted from the work of Rizzo et al. (2006). The images in this work also indicate a flat contact surface of the pad, which is considered here<sup>4</sup>. Further spatula images can be found in Autumn et al. (2000); Arzt et al. (2003); Huber et al. (2005); Autumn et al. (2006); Tian et al. (2006). The shaft diameter is on the order of 100 nm and tends to be tapered towards the pad. The pad is very thin, typically only around 10 nm thick, which gives it great flexibility to adapt to the roughness of the substrate it attaches to. The rim of the pad is considerably thicker, probably to give the entire structure higher stability. Fig. 1.b shows the idealized spatula model that is proposed here. The model captures the essential details of the geometry of the spatula shaft, pad and rim geometry. The geometric model is based on a set of parameters and construction rules discussed in the following. This description is an advancement of the description considered in Sauer (2009), which models the spatula as a 2D beam with varying cross-section. The new 3D spatula model is shown schematically in Fig. 2. The geometry is based on 15 points, denoted

---

<sup>4</sup>Further measurements are called for in order to determine the details of the spatula geometry

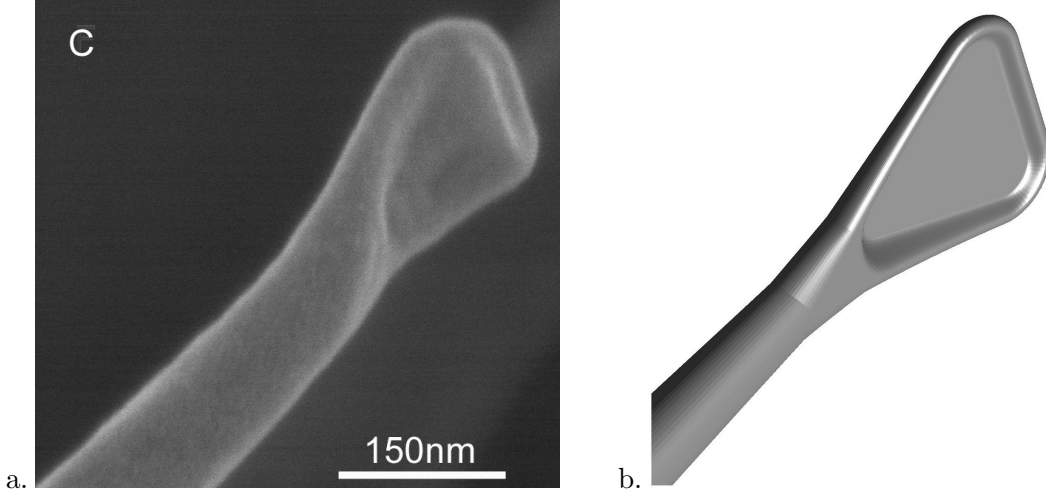


Figure 1: The gecko spatula: microscope image (left; adopted with permission from J. R. Soc. Interface (Rizzo et al., 2006)) and idealized 3D model considered here (right).

$P_1$  to  $P_{15}$ , which are defined in Tab. 1, and on the following related geometrical parameters:

- $c_s$ , the radius of the circular cross-section of the shaft end face (at  $P_1$ ),
- $a_s$  and  $b_s$ , the half-widths of the elliptical shaft cross-section at location  $P_2$ , the designated connection between shaft and pad,
- $\ell_s$ , the shaft length measured along the center axis from the end face (at  $P_1$ ) to the connection at  $P_2$ ,
- $\theta_s$ , the inclination of the center axis of the shaft w.r.t. the  $\{X, Y\}$ -plane,
- $r_5$ , the radius that describes the  $Z$ -coordinate of the curve passing through  $P_2$  to  $P_7$ ,
- $\ell_p$ , the pad length (the  $X$ -distance between  $P_2$  and  $P_7$ ),
- $w_p$ , the pad width (the  $Y$ -diameter of the pad at  $P_{13}$  up to the arc through  $P_5$  and  $P_6$ ),
- $h_p$ , the pad thickness,
- $h_r$ , the rim thickness at the tip (chosen here as  $h_r = 2h_p$ ),
- the pad corner radii  $r_1$  (the distance from  $P_{13}$  to  $P_5$ ),  $r_2$  (the distance from  $P_{13}$  to  $P_9$ ),  $r_3$  (the distance from  $P_{14}$  to  $P_4$ ) and  $r_4$  (the distance from  $P_{14}$  to  $P_{10}$ ).

To facilitate the description of the spatula geometry, it is broken into four parts, denoted  $\mathcal{P}_I$ ,  $\mathcal{P}_{II}$ ,  $\mathcal{P}_{III}$  and  $\mathcal{P}_{IV}$ , as shown in Fig. 2. These parts are then also used for the meshing discussed below (see Fig. 3). A detailed description of the geometry of parts  $\mathcal{P}_I$ ,  $\mathcal{P}_{II}$ ,  $\mathcal{P}_{III}$  and  $\mathcal{P}_{IV}$  is given in Appendix A. The coordinates of points  $P_1$  to  $P_{15}$ , used here, are given in Tab. 1. These coordinates follow from the choice of the model parameters given in Tab. 2. From these parameters follows  $r_5 = 4081$  nm and  $\theta_s = 4.91^\circ$ . Choosing other parameters will lead to different spatula shapes.

The spatula geometry is meshed using hexahedral tri-linear solid finite elements as is shown in Fig. 3. To avoid excessive mesh distortion at point  $P_2$ , the boundary between part  $\mathcal{P}_I$  and  $\mathcal{P}_{III}$  has to be slightly shifted along the  $X$ -axis at this point. This shift only affects the mesh but not the spatula geometry. Care is needed to ensure that all the finite element nodes connect to each other properly at the interfaces between the four parts. For this study three different mesh densities were initially considered. The number of elements for each is shown in Tab. 3. The contact surface of the pad is formed by the bottom surface of parts  $\mathcal{P}_{II}$ ,  $\mathcal{P}_{III}$  and  $\mathcal{P}_{IV}$ , where

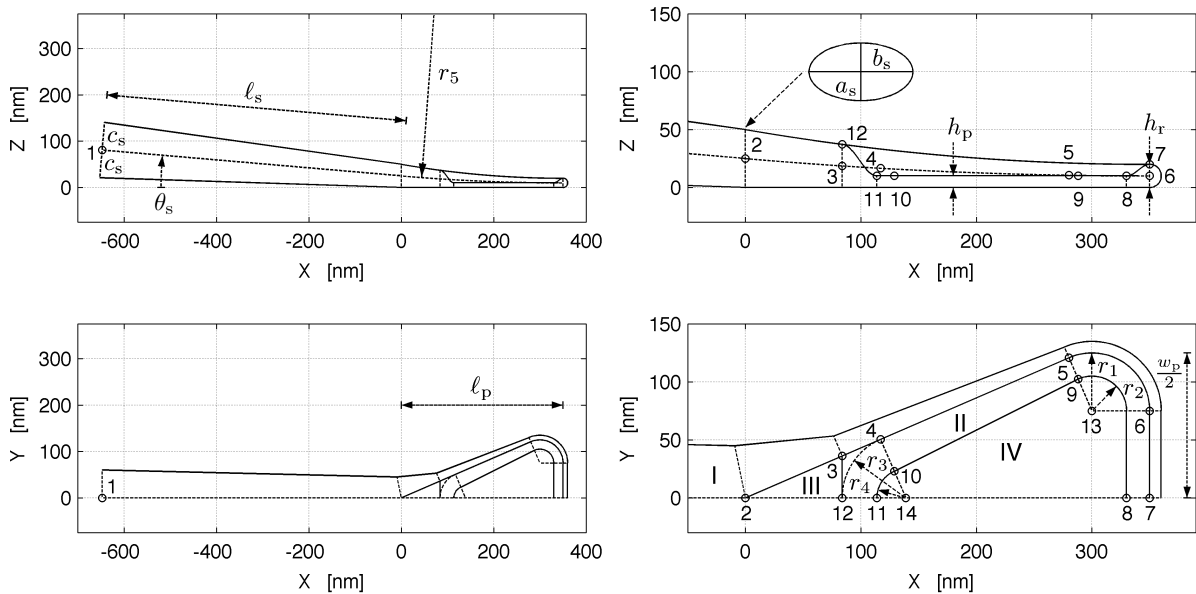


Figure 2: Side view (top row) and top view (bottom row) of the proposed spatula geometry model. Points  $P_1$  to  $P_{14}$  are defined in Tab. 1. Regions  $\mathcal{P}_{II}$  and  $\mathcal{P}_{IV}$  form the pad; regions  $\mathcal{P}_I$  and  $\mathcal{P}_{III}$  form the shaft and the rim of the pad.

$Z = 0$  (see Fig. 2). The finite elements located on this surface are used to describe the adhesion between pad and substrate according to the 3D formulation of Sauer and Wriggers (2009). The total number of contact elements in the mesh is provided in Tab. 3 along with the largest characteristic element size among those contact surface elements. It turns out that the first two meshes are inadequate to describe the adhesion forces properly: The computations are not stable and therefore fail.<sup>5</sup> The mesh density on the contact surface is simply too coarse to capture the adhesion forces adequately: According to the adhesion parameters considered here (see Sec. 3) the maximum attraction occurs at a surface distance of 0.306 nm (Sauer and Wriggers, 2009). Therefore, even the fine mesh may produce poor results during peeling computations (Sauer, 2011a). One possibility is to use even finer meshes, for example by subdividing each hexahedral element into 8 new elements, so that the maximum contact diameter will be halved. However this will increase the computational cost dramatically. A much better and highly efficient strategy is to enrich the finite element approximation on the contact surface as proposed in Sauer (2011a). This contact enrichment technique, which is used here, is outlined in the following section. The enrichment formulation does not change the total number of elements.

### 3 The adhesion formulation

This section outlines the computational formulation used to model van der Waals adhesion between the gecko spatula pad and a rigid substrate. The formulation is based on the contact model of Sauer and Li (2007). The Lennard-Jones potential is used to describe the van der Waals interaction between the molecules of the neighboring bodies. In this case, the adhesive contact tractions acting on the deformed spatula pad  $\mathcal{B}_1$ , due to the interaction with the substrate  $\mathcal{B}_2$ ,

<sup>5</sup>Even though the coarse and medium meshes are not suitable to capture adhesion they can be employed to study the structural properties of the spatula, like its vibration modes (Sauer, 2012b).

	$X$ [nm]	$Y$ [nm]	$Z$ [nm]
$P_1$	-647.6	0.0	80.6
$P_2$	0.0	0.0	25.0
$P_3$	83.8	36.2	18.7
$P_4$	117.0	50.5	16.6
$P_5$	280.2	120.9	10.6
$P_6$	350.0	75.0	10.0
$P_7$	350.0	0.0	20.0
$P_8$	330.0	0.0	10.0
$P_9$	288.1	102.5	10.0
$P_{10}$	128.9	23.0	10.0
$P_{11}$	113.8	0.0	10.0
$P_{12}$	83.8	0.0	37.3
$P_{13}$	300.0	75.0	-
$P_{14}$	138.8	0.0	-
$P_{15}$	350	-	4,091

Table 1: Coordinates of the points displayed in Fig. 2.

shaft	$a_s = 25,$	$b_s = 45,$	$c_s = 60,$	$\ell_s = 650$
pad	$\ell_p = 350,$	$h_p = 10,$	$h_r = 20,$	$w_p = 250$
radii	$r_1 = 50,$	$r_2 = 30,$	$r_3 = 55,$	$r_4 = 25$

Table 2: Geometric parameters of the spatula model, in units of nanometers.

are given by

$$\mathbf{t}_1(r_s, \mathbf{n}_2) = \pi\beta_1\beta_2\epsilon r_0^3 \left[ \frac{f_1}{45} \left(\frac{r_0}{r_s}\right)^9 - \frac{f_2}{3} \left(\frac{r_0}{r_s}\right)^3 \right] \cos \alpha_1 \mathbf{n}_2 . \quad (1)$$

At a given surface location  $\mathbf{x}_s$  on the spatula pad, the traction  $\mathbf{t}_1$  depends on the distance,  $r_s$ , and surface orientation,  $\mathbf{n}_2$ , of the neighboring substrate surface  $\partial\mathcal{B}_2$ . For flat substrate surfaces, direction  $\mathbf{n}_2$  is constant and the distance  $r_s$  can be easily evaluated.  $\alpha_1$  denotes the relative angle between the two surfaces of  $\mathcal{B}_1$  and  $\mathcal{B}_2$ , which, in general, are not parallel. This, for example, is the case in the peeling zone. The two factors  $f_1$  and  $f_2$  dependent on the surface curvature of the substrate surfaces (Sauer and Wriggers, 2009). For a flat or only moderately curved substrate surface, as considered in the examples in Sec. 4, we have  $f_1 \approx f_2 \approx 1$ . Expression (1) can be derived from the global interaction energy (Sauer and Wriggers, 2009)

$$\Pi_c = \int_{\mathcal{B}_1} \int_{\mathcal{B}_2} \beta_1\beta_2 \phi(r) dv_2 dv_1 , \quad (2)$$

where  $\beta_k$  is the current molecular density of body  $\mathcal{B}_k$ , and where  $\phi$  denotes the Lennard-Jones potential

$$\phi(r) := \epsilon \left(\frac{r_0}{r}\right)^{12} - 2\epsilon \left(\frac{r_0}{r}\right)^6 , \quad (3)$$

that governs the interaction between two molecules separated by  $r$  and depends on two material parameters: The length scale  $r_0$  and the energy scale  $\epsilon$ . In principle the contact tractions according to (1) are valid for arbitrarily separated and oriented surface elements. For actual computations, however, it is useful to consider a cut-off radius for the surface distance  $r_s$ , beyond which the adhesion forces are neglected. According to formulation (1), the local contact tractions acting on the spatula pad are normal to the substrate surface, i.e.  $\mathbf{t}_1$  is parallel to  $\mathbf{n}_2$ . For perfectly smooth substrate surfaces the model is thus frictionless. Sliding and sticking

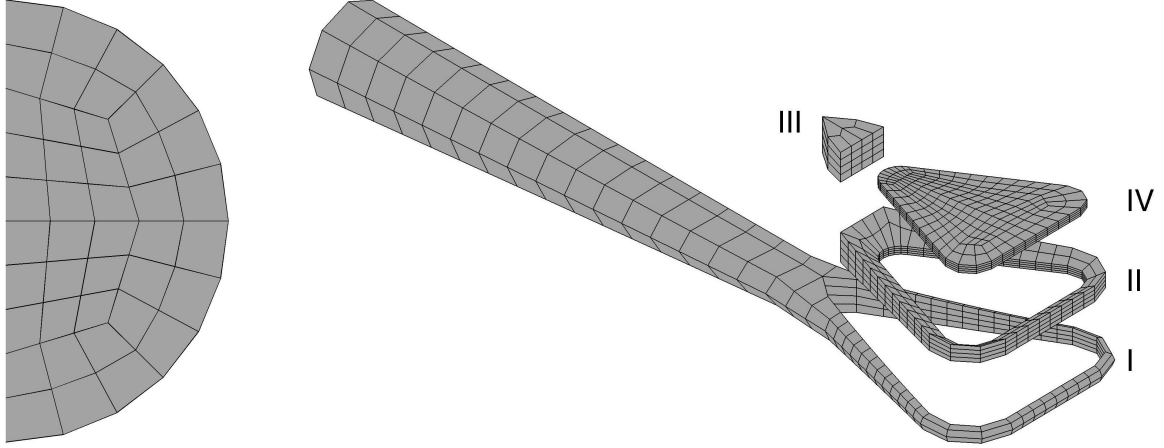


Figure 3: Finite element discretization of the spatula end face using the fine mesh of Tab. 3 (left); FE discretization of the four spatula parts using the coarse mesh of Tab. 3 (right). For the medium and fine mesh every surface element of the pad is broken into  $4 \times 4$  and  $8 \times 8$  new elements.

	$\mathcal{P}_I$	$\mathcal{P}_{II}$	$\mathcal{P}_{III}$	$\mathcal{P}_{IV}$	total	contact	diameter
coarse	228	168	12	376	784	139	22.39
medium	912	2,688	192	6,016	9,808	2,224	5.71
fine	12,768	26,880	1,920	60,160	101,728	8,896	2.87

Table 3: Number of solid elements and contact elements in the FE model (for half of the spatula); largest diameter of the contact elements (in nanometers).

friction can be modeled considering a rough substrate surface and dissipative material response (Wriggers and Reinelt, 2009). Such an approach is outside the scope of the present study. Alternatively, tangential sticking forces can also be modeled by a cohesive interface law (Xu and Needleman, 1993). The peeling examples in Sec. 4 are chosen such that no tangential loading is present in the contact interface. It is shown that for these loading cases sticking forces play a negligible role in the peeling behavior.

For the present study, we consider a rigid substrate and quasi-static behavior. In this case the weak form governing the mechanical behavior of the spatula is given by

$$\int_{\mathcal{B}_1} \text{grad}(\delta\varphi_1) : \boldsymbol{\sigma}_1 \, dv_1 - \int_{\partial\mathcal{B}_1} \delta\varphi_1 \cdot \mathbf{t}_1 \, da_1 - \delta\Pi_{\text{ext},1} = 0 \quad \forall \delta\varphi_1 \in \mathcal{V}_1, \quad (4)$$

where  $\mathcal{V}_1$  denotes the space of kinematically admissible variations  $\delta\varphi_1$  and where  $\delta\Pi_{\text{ext},1}$  accounts for external forces prescribed on the spatula, which are considered zero in all following examples, i.e.  $\delta\Pi_{\text{ext},1} = 0$ . The first contribution denotes the internal virtual work of the Cauchy stress  $\boldsymbol{\sigma}_1$ , which is derived from the potential

$$\Pi_{\text{int}} = \int_{\mathcal{B}_{01}} W_1(\mathbf{F}_1) \, dV_1, \quad (5)$$

where  $W_1$  denotes the stored energy function of body  $\mathcal{B}_1$ , which depends on the deformation gradient  $\mathbf{F}_1 = \partial\varphi_1/\partial\mathbf{X}_1$  of the deformation  $\mathbf{x}_1 = \varphi_1(\mathbf{X}_1)$  of  $\mathcal{B}_1$ . The stress tensor  $\boldsymbol{\sigma}_1$  is then obtained as

$$\boldsymbol{\sigma}_1 = \frac{1}{J_1} \frac{\partial W_1}{\partial \mathbf{F}_1} \mathbf{F}_1^T, \quad (6)$$

where  $J_1 = \det \mathbf{F}_1$ . In this paper a nonlinear, Neo-Hookean material model of the form

$$W_1 = \frac{\Lambda}{2} (\ln J_1)^2 + \frac{\mu}{2} (\text{tr}(\mathbf{F}_1 \mathbf{F}_1^T) - 3) - \mu \ln J_1, \quad (7)$$

is considered. The Lamé parameters  $\Lambda$  and  $\mu$  can be obtained from Young's modulus  $E$  and Poisson's ratio  $\nu$  using

$$\mu = \frac{E}{2(1+\nu)}, \quad \Lambda = \frac{2\mu\nu}{1-2\nu}. \quad (8)$$

For the Neo-Hooke material model the Cauchy stress tensor follows as

$$\boldsymbol{\sigma}_1 = \frac{\Lambda}{J_1} \ln J_1 \mathbf{I} + \frac{\mu}{J_1} (\mathbf{F}_1 \mathbf{F}_1^T - \mathbf{I}), \quad (9)$$

where  $\mathbf{I}$  denotes the identity tensor. The adhesion model according to eqs. (4), (9) and (1) is a nonlinear deformation model that fully accounts for the geometrical and material nonlinearities of large deformations. It can be viewed as a coupling of the elastic deformation with the intersurface adhesion forces. It is solved simultaneously for the unknown spatula deformation  $\boldsymbol{\varphi}_1$ . Therefore, boundary conditions need to be provided. In the examples of Sec. 4, the following two sets of boundary conditions are considered:

1. Applying a rotation at the end face of the shaft while considering a zero net force acting on the end face.
2. Applying a displacement at the end face, which is normal to the substrate surface, while considering a zero net moment acting on the end face.

These conditions are useful since they allow the investigation of the spatula response for different shaft positions and inclinations, as they would, in reality, be determined by the gecko seta and gecko foot, where the spatulae are attached to.

Given a finite element discretization of the pad surface, the force vector acting on the  $n_e$  nodes of surface element  $\Gamma_e$  is given by (Sauer and Wriggers, 2009)

$$\mathbf{f}_c^e := - \int_{\Gamma_e} \mathbf{N}_e^T \mathbf{t}_1 da_1, \quad (10)$$

where

$$\mathbf{N}_e = [N_1 \mathbf{I}, N_2 \mathbf{I}, \dots, N_{n_e} \mathbf{I}] \quad (11)$$

is a  $(3 \times 3n_e)$  matrix formed by the  $n_e$  shape functions  $N_I$  ( $I = 1, 2, \dots, n_e$ ) of the surface element. Integration (10) is carried out over the current (i.e. deformed) configuration of the pad surface. Alternatively, the integral can be transformed to the undeformed reference configuration using Nanson's formula

$$\mathbf{n}_1 da_1 = J_1 \mathbf{F}_1^{-T} \mathbf{N}_1 dA_1, \quad (12)$$

where  $dA_1$  denotes a surface element with the orientation  $\mathbf{N}_1$  in the undeformed reference configuration, and  $da_1$  denotes the corresponding surface element with the orientation  $\mathbf{n}_1$  in the deformed configuration. With (12), the finite element force vector becomes

$$\mathbf{f}_c^e := - \int_{\Gamma_{e0}} \mathbf{N}_e^T \mathbf{T}_1 dA_1, \quad (13)$$

where  $\Gamma_{e0}$  denotes the undeformed configuration of the surface element. The traction  $\mathbf{T}_1$ , which follows from eq. (1), is given by (Sauer and Wriggers, 2009)

$$\mathbf{T}_1 := \pi \beta_{01} \beta_\ell \epsilon r_0^3 \left[ \frac{1}{45} \left( \frac{r_0}{r_s} \right)^9 - \frac{1}{3} \left( \frac{r_0}{r_s} \right)^3 \right] \theta_1 \mathbf{n}_2 \quad (14)$$

with

$$\theta_1 := -\mathbf{n}_2 \cdot \mathbf{F}_1^{-T} \mathbf{N}_1 . \quad (15)$$

As shown in [Sauer and Wriggers \(2009\)](#), the parameter  $\theta_1$  can be approximated as  $\theta_1 = 1$  for even moderately strong adhesion, as is the case for gecko adhesion. Introducing Hamaker's constant  $A_H = 2\pi^2\beta_{01}\beta_{02}\epsilon r_0^6$  ([Israelachvili, 1991](#)), where  $\beta_{0k} = J_k\beta_k$  denotes the particle density in the undeformed reference configuration  $\mathcal{B}_{0k}$  ( $k = 1, 2$ ), the traction  $\mathbf{T}_1$  can then also be written as

$$\mathbf{T}_1 = \frac{A_H}{2\pi r_0^3 J_2} \left[ \frac{1}{45} \left( \frac{r_0}{r_s} \right)^9 - \frac{1}{3} \left( \frac{r_0}{r_s} \right)^3 \right] \mathbf{n}_2 . \quad (16)$$

Since the substrate is considered rigid, we have  $J_2 = 1$ .

The stiffness matrix associated with the force vector  $\mathbf{f}_c^e$  is given by the symmetric,  $(3n_e \times 3n_e)$  matrix ([Sauer and Wriggers, 2009](#))

$$\mathbf{k}_c^e = - \int_{\Gamma_{e0}} \mathbf{N}_e^T \frac{\partial \mathbf{T}_1}{\partial \mathbf{x}_1} \mathbf{N}_e dA_1 , \quad (17)$$

with

$$\frac{\partial \mathbf{T}_1}{\partial \mathbf{x}_1} = - \frac{A_H}{2\pi r_0^4} \left[ \frac{1}{5} \left( \frac{r_0}{r_s} \right)^{10} - \left( \frac{r_0}{r_s} \right)^4 \right] \mathbf{n}_2 \otimes \mathbf{n}_2 . \quad (18)$$

This expression is only valid for rigid, flat substrate surfaces with  $\theta_1 = 1$ , as is considered here. In general, further terms are picked up, as is shown in [Sauer \(2012a\)](#). There, the finite element algorithm, used to solve the present contact formulation, is also discussed.

The model, governed by eq. (4), is mainly characterized by two material parameters, the ratios

$$\gamma_L = \frac{R_0}{r_0} , \quad \gamma_W = \frac{W_0}{w_0} , \quad (19)$$

which can be identified from a normalization of eq. (4) ([Sauer and Li, 2008](#)). The length  $R_0$  is a global length scale used to normalize the spatula geometry.  $\gamma_L$  then characterizes the overall size of the spatula with respect to the range of adhesion.  $W_0$  and  $w_0$  denote two energy densities that correspond to the energy stored in the elastic deformation and in the adhesion. The densities can be defined as

$$W_0 = E , \quad w_0 = \frac{A_H}{2\pi^2 r_0^3} , \quad (20)$$

where  $E$  and  $A_H$  denote Young's modulus and Hamaker's constant. According to the definition of Hamaker's constant,  $w_0$  can also be written as  $w_0 = \beta_{01}\beta_{02}\epsilon r_0^3$ .  $\gamma_W$  characterizes the strength of adhesion in relation to the stiffness of the spatula: For smaller  $\gamma_W$  the adhesion becomes stronger. The basic material parameters used in the following examples are  $E = 2$  GPa,  $\nu = 0.2$ ,  $A_H = 10^{-19}$  J and  $r_0 = 0.4$  nm, which correspond to the values considered by previous authors ([Israelachvili, 1991](#); [Tian et al., 2006](#); [Sauer, 2009](#)). Setting  $R_0 = 1$  nm we thus have

$$\gamma_{L0} = 2.5 , \quad \gamma_{W0} = 25.266 . \quad (21)$$

The subscript '0' is used to distinguish this particular choice from the variations examined in [Sec. 4.4](#).

The presented three-dimensional spatula model is capable of capturing the details of the contact behavior. This is shown in [Fig. 4](#), which visualizes the stress component  $I_1 = \text{tr } \boldsymbol{\sigma}$  on the spatula surface considering the model parameters  $\gamma_L = \gamma_{L0}$  and  $\gamma_W = \gamma_{W0}$ . It can be seen that strong adhesive stresses appear in a very narrow band which indicates the location of the peeling zone.

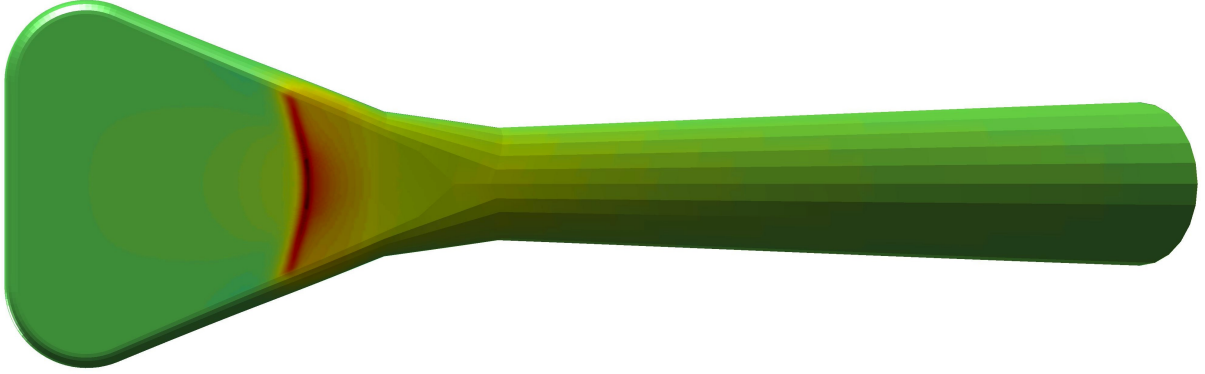


Figure 4: Adhesive contact stresses at the underside of the spatula pad for a shaft inclination of  $45^\circ$  (see section 4). The colors show the stress component  $I_1 = \text{tr } \boldsymbol{\sigma}$  in the same scale used in Fig. 5. Shown is the undeformed spatula configuration.

The maximum adhesive surface traction that occurs in the peeling zone is given by the global minimum of expression (1), which is

$$t_{\min} = \|\mathbf{t}_1(r_{\min})\| = \sqrt{5} \frac{A_H}{9\pi J_1 r_0^3}, \quad r_{\min} = \sqrt[6]{1/5} r_0. \quad (22)$$

Here, the parameter  $J_1 = \det \mathbf{F}_1$  describes the volume change of the deformation of the pad. Since the pad is usually stretched in the peeling zone, we can expect that  $J_1 \geq 1$  there, and we can obtain an upper bound on the maximum peeling stress by setting  $J_1 = 1$  in eq. (22). Fig. 4 shows that the presented adhesion model constitutes a more detailed model formulation than the analytical models of Johnson et al. (1971) and Kendall (1975), which are formulated for elastic spheres and thin films. Since the spatula structure is neither a sphere nor a thin film (the thickness has a strong influence on spatula peeling (Sauer, 2011b)), the Johnson et al. model over- and the Kendall model underestimates the peeling forces.

Since the strongest peeling forces are only located within a very narrow band, a sufficiently fine finite element surface discretization is needed in order to resolve the peeling forces and thus compute the peeling process accurately. If the mesh is too coarse, the computations become inaccurate and possibly also unstable (Sauer, 2011a). Instead of simply refining the finite element mesh within the peeling zone, one can also consider an enrichment of the contact surface description (Sauer, 2011a). Such a formulation produces highly accurate contact forces, while the overall numerical cost is still kept very low. The simplest enrichment idea is to use quadratic interpolation on the contact surface but standard linear interpolation everywhere else. This finite element contact formulation is denoted as Q1C2 in Sauer (2011a). A standard finite element formulation, that uses linear interpolation on the contact surface and elsewhere, would then correspond to a Q1C1 element formulation. The enriched contact element formulation Q1C2 is used for all computations presented here.

As a final consideration, the energy required to remove the adhering spatula from the substrate is discussed. This energy can be computed from the work of adhesion  $w_{\text{adh},\infty}$  that is defined as (Israelachvili, 1991)

$$w_{\text{adh},\infty} := - \int_{r_{\text{eq}}}^{\infty} \|\mathbf{T}_1\| dr_s = \sqrt[3]{15} \frac{A_H}{16\pi r_0^2}, \quad (23)$$

i.e. it denotes the work required to remove two bodies with reference contact surface  $dA$  from

the equilibrium position  $r_s = r_{\text{eq}}$  (where  $\|\mathbf{T}_1\| = 0$ ) to  $r_s = \infty$ .<sup>6</sup> The energy required to completely remove the spatula from the substrate then follows from integrating  $w_{\text{adh},\infty}$  over the total, undeformed surface area adhering to the substrate, denoted as  $A_c$ . We thus obtain the limit value  $\Pi_{c,0} := A_c w_{\text{adh},\infty}$ . For the spatula model described in Sec. 3, the entire contact area is  $A_c = 49,524 R_0^2$ . For the parameters considered here, we thus find  $\Pi_{c,0} = 759.3 ER_0^3$ .<sup>7</sup> It is noted that the true energy required to remove the adhering spatula can be considerably larger, i.e.  $\Pi_{c,0}$  is only a lower bound, since some energy will be dissipated in the system. The quantity  $\Pi_{c,0}$  corresponds to (the absolute value of) the minimum of potential  $\Pi_c$  (2), which is attained for the initial configuration of the adhering spatula. As the spatula is removed from the substrate,  $\Pi_c$  thus increases from  $-\Pi_{c,0}$  to 0. The amount of external work required for the removal process, which is stored in the adhesion interface, is thus given as

$$\Pi_{\text{sa}} = \Pi_{c,0} + \Pi_c . \quad (24)$$

As the spatula is removed from the substrate,  $\Pi_{\text{sa}}$  increases from 0 to  $\Pi_{c,0}$ . This can be seen in the numerical examples considered in the following section. For conservative systems we then have  $\Pi_{\text{ext}} = \Pi_{\text{int}} + \Pi_{\text{sa}}$ , where  $\Pi_{\text{ext}}$  denotes the external work applied for the removal process. It is fully recovered upon unloading. (For non-conservative systems a part of  $\Pi_{\text{ext}}$  is not recovered upon unloading.)

## 4 The adhesion behavior

This section discusses the adhesive behavior of the gecko spatula for a range of different loading conditions and model parameters. The first case studies the peeling of the spatula by applying a rotation to the shaft. The second case studies the spatula detachment by an applied displacement. Various shaft inclinations and adhesion parameters are therefore considered. Finally, to demonstrate the capabilities of the presented spatula model, the adhesion of the spatula to a rough surface is examined. The subscripts used in the following correspond to the coordinate system introduced in Sec. 2:  $\theta_y$  and  $M_y$  denote the rotation and moment component in the  $y$ -direction, which is the direction perpendicular to the shaft axis and parallel to the substrate surface;  $u_z$  and  $P_z$  denote the displacement and force component in the direction normal to the substrate surface.

### 4.1 Spatula peeling by an applied rotation

By applying a rotation to the end face of the shaft, the spatula peels-off the substrate, as is shown in Fig. 5. In this case, the end face of the shaft is considered free to move in the  $z$ -direction. Due to the symmetry of the system, only half of the spatula is modeled. At the peeling front large tensile stresses develop on the bottom surface of the pad while compressive bending stresses occur on the top. The computation shows the advancement of the peeling front across the pad surface. In the initially undeformed configuration the shaft has an inclination of  $\theta_y = \theta_s = 4.91^\circ$  (see Sec. 2). For the considered parameters, the shaft can support rotations up to  $130^\circ$  before detachment.

Fig. 6 shows the moment  $M_y$  that is required to apply the rotation. The moment during

<sup>6</sup>Strictly, this parameter can only be used to describe surface regions that have fully separated from the substrate. For regions that have only partially separated, the work of adhesion also depends on the inclination of the surface (Sauer, 2011b).

<sup>7</sup>In the computations reported here, the contact force  $\mathbf{T}_1$  is modified in the compression regime, in order to regularize the function for low  $r_s$  (Sauer, 2011a). Due to this modification the actual value is  $\Pi_{c,0} = 761.5 ER_0^3$ .

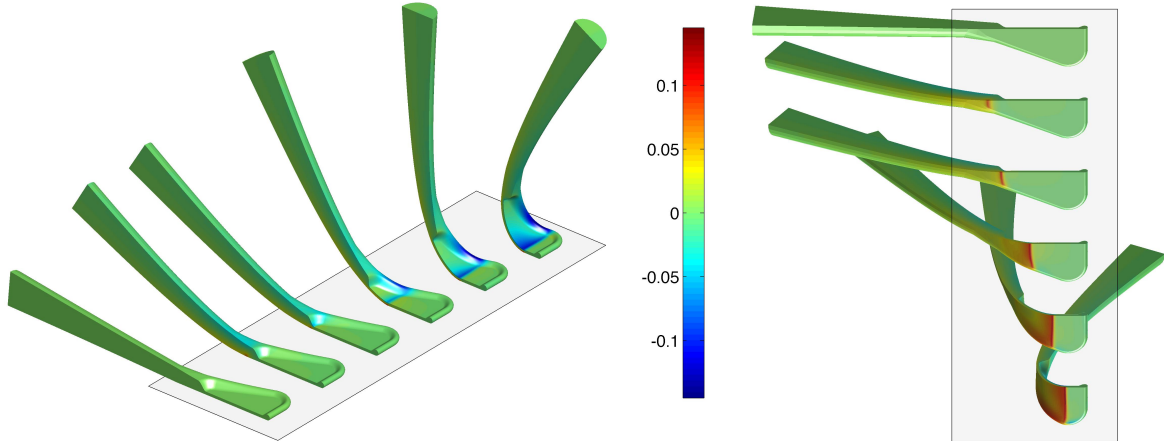


Figure 5: Spatula peeling due to an applied rotation of the shaft: Top view on the left, bottom view on the right. Shown are the configurations for prescribed shaft inclinations of  $\theta_y = 4.9^\circ$ ,  $31^\circ$  (twice),  $60^\circ$ ,  $90^\circ$ ,  $120^\circ$ . The colors show  $I_1 = \text{tr } \boldsymbol{\sigma}$  normalized by Young's modulus  $E$ .

peeling is not constant as is the case for thin films with constant thickness (Sauer, 2011b). At an inclination of  $31^\circ$  the moment drops sharply due to an instability in the system: At the connection between spatula shaft and pad the bending stiffness decreases quite abruptly, which causes the shown moment drop. In Fig. 6, the moment  $M_y$  is normalized by  $ER_0^3$ . Given the model parameters considered here ( $E = 2 \text{ GPa}$ ,  $R_0 = 1 \text{ nm}$ ), we have  $ER_0^3 = 2 \text{ nNm}$ .

The external work that is applied on the structure corresponds to the area under the  $M_y(\theta_y)$  curve, i.e.

$$\Pi_{\text{ext}}(\theta_y) = \int_{\theta_s}^{\theta_y} M_y(\bar{\theta}_y) d\bar{\theta}_y. \quad (25)$$

This work is stored in the elastic strain energy  $\Pi_{\text{int}}$  and in the adhesion energy  $\Pi_{\text{sa}}$  defined in eqs. (5) and (24). Tab. 4 shows the values of  $\Pi_{\text{ext}}$ ,  $\Pi_{\text{int}}$  and  $\Pi_{\text{sa}}$  relative to the maximum adhesion energy  $\Pi_{c,0}$  given in Sec. 3. As expected  $\Pi_{\text{int}} + \Pi_{\text{sa}} = \Pi_{\text{ext}}$  (up to a numerical error of

$\theta_y$	$\Pi_{\text{ext}}/\Pi_{c,0}$	$\Pi_{\text{int}}/\Pi_{c,0}$	$\Pi_{\text{sa}}/\Pi_{c,0}$
$30^\circ$	0.237	0.222	0.013
$31^\circ -$	0.255	0.232	0.021
$31^\circ +$	0.255	0.182	0.071
$60^\circ$	0.689	0.395	0.291
$90^\circ$	1.088	0.545	0.540
$120^\circ$	1.455	0.728	0.724
$128^\circ$	1.551	0.738	0.811

Table 4: Applied external work  $\Pi_{\text{ext}}$  and stored energies  $\Pi_{\text{int}}$  and  $\Pi_{\text{sa}}$  for different shaft inclinations  $\theta_y$ . For  $E = 2 \text{ GPa}$  and  $R_0 = 1 \text{ nm}$  we have  $\Pi_{c,0} = 1.523 \cdot 10^{-15} \text{ J}$ .

about  $0.002 \Pi_{c,0}$ ). It can be seen that for low  $\theta_y$ , nearly all the applied energy is transformed into elastic energy  $\Pi_{\text{int}}$ . Beyond the instability the amount of applied energy that is transformed into the contact energy  $\Pi_{\text{sa}}$  increases strongly. At detachment ( $\theta_y = 128^\circ$ ), the contact energy is still not saturated ( $\Pi_{\text{sa}} < \Pi_{c,0}$ ): About 19% of the pad is still adhering to the substrate. When the spatula detaches from the substrate, the energy  $\Pi_{\text{int}}$  will be released, leading to the vibration of the structure. We note that the stored contact energy  $\Pi_{\text{sa}}$  is approximately proportional to the region of the pad that has detached. However, it is not exactly proportional since, due to

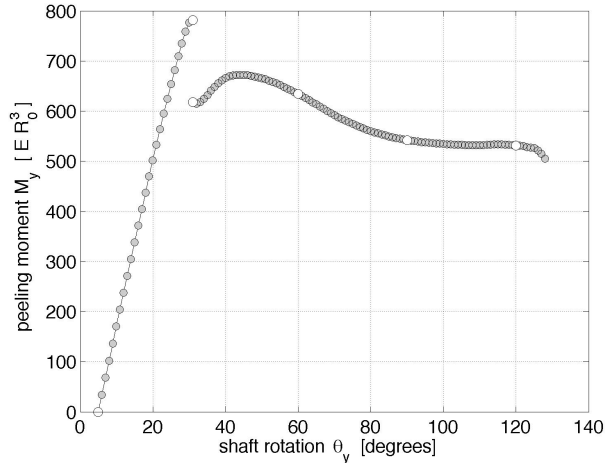


Figure 6: Moment-rotation curve for peeling by an applied rotation. The white dots mark the six configurations shown in Fig. 5. An instability occurs at  $\theta_y = 31^\circ$ .

the long range van der Waals interaction, parts of the separated pad will still contribute to the adhesion.

## 4.2 Spatula peeling force for various shaft inclinations

The spatula can also be detached from the substrate by considering a displacement  $u_z$  normal to the substrate surface. This is analyzed here for various fixed shaft inclinations (i.e. a fixed rotation is maintained at the end face). These pre-rotated starting configurations are taken from the computation reported in the previous section. They account for different relative positions between spatula shaft and substrate and thus account for either inclined spatulae or locally slanted substrate surfaces.

Fig. 7 shows the deformation of the spatula during pull-off for a fixed end face rotation of  $60^\circ$ . The stresses inside the structure are lower than in the case of peeling by rotation. The force  $P_z$ , required to apply the displacement  $u_z$ , is shown in Fig. 8 for the shaft inclinations  $\theta_y = 45^\circ, 60^\circ, 75^\circ$  and  $\theta_y = 90^\circ$ . Here, the coordinate  $u_z$  measures the  $z$ -displacement of the center of the shaft end face starting from the completely undeformed configuration. In each case the pull-off force<sup>8</sup> increases almost linearly up to a maximum value, which is reached just prior to detachment. These maximum pull-off forces lie in the range between 4 nN and 8 nN, and they decrease with increasing  $\theta_y$ . These results are in agreement to the measured forces of Huber et al. (2005) and Sun et al. (2005) and to the computational result of Sauer (2009), which is based on a reduced beam model for the spatula. The pull-off force during peeling is not constant as is the case for thin films with negligible thickness (Kendall, 1975).

Additional external work is required to pull-off the spatula from the considered pre-rotated configurations. It is equal to the area under the load-displacement curve, i.e.

$$\Delta\Pi_{\text{ext}}(u_z) = \int_{u_0}^{u_z} P_z(\bar{u}_z) d\bar{u}_z . \quad (26)$$

<sup>8</sup>Here, the terminology ‘pull-off force’ is used to denote the varying, displacement-dependent force during the pull-off process.

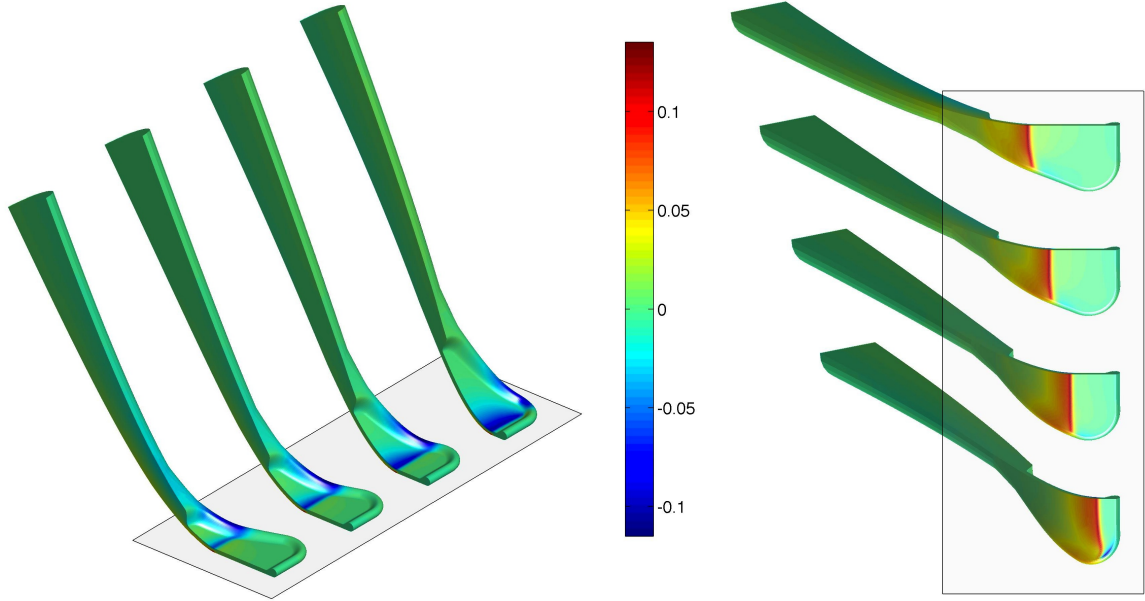


Figure 7: Spatula deformation for an applied vertical pull-off displacement  $u_z$  considering a fixed shaft inclination of  $\theta_y = 60^\circ$ . The colorscale shows  $I_1 = \text{tr } \boldsymbol{\sigma}$  normalized by  $E$ .

where  $u_0$  denotes the pre-rotated initial configuration (where  $P_z = 0$ ). The values of  $\Delta\Pi_{\text{ext}}$  are given in Tab. 5 together with stored energies  $\Pi_{\text{int}}$  and  $\Pi_{\text{sa}}$ . As expected  $\Pi_{\text{int}} + \Pi_{\text{sa}} =$

$\theta_y$	$\Pi_{\text{ext},0}/\Pi_{c,0}$	$\Delta\Pi_{\text{ext}}/\Pi_{c,0}$	$\Pi_{\text{ext}}/\Pi_{c,0}$	$\Pi_{\text{int}}/\Pi_{c,0}$	$\Pi_{\text{sa}}/\Pi_{c,0}$
$45^\circ$	0.463	0.720	1.184	0.316	0.865
$60^\circ$	0.689	0.460	1.149	0.242	0.905
$75^\circ$	0.897	0.277	1.174	0.249	0.923
$90^\circ$	1.088	0.154	1.242	0.319	0.920

Table 5: Applied additional work  $\Delta\Pi_{\text{ext}}$  and total stored energy  $\Pi_{\text{int}}$  and  $\Pi_{\text{sa}}$  prior to detachment considering an applied vertical displacement  $u_z$  and fixed shaft inclinations  $\theta_y$ . For  $E = 2 \text{ GPa}$  and  $R_0 = 1 \text{ nm}$  we have  $\Pi_{c,0} = 1.523 \cdot 10^{-15} \text{ J}$ .

$\Pi_{\text{ext},0} + \Delta\Pi_{\text{ext}} := \Pi_{\text{ext}}$  (up to a numerical error of about  $0.002 \Pi_{c,0}$ ), where  $\Pi_{\text{ext},0}$  denotes the work of the pre-applied rotation. The concrete values of the applied pull-off work  $\Delta\Pi_{\text{ext}}$  are shown in Tab. 6. This table also provides the concrete values of the maximum pull-off force and the displacement at detachment. It can be seen that these measures decrease with increasing  $\theta_y$ .

### 4.3 Influence of tangential stiction forces

The computational results shown in the previous section consider frictionless contact behavior. Frictional contact forces are activated if relative tangential motion occurs across the contact interface. In the following, a simple frictional contact model is considered and it is shown that its influence on the considered peeling behavior is very small. Contact law (16), considered so far, only provides a normal contact force based on the normal contact distance  $r_s$ . As a simple extension, consider

$$\mathbf{T}_1 = \frac{A_H}{2\pi r_0^3} \left[ \frac{1}{45} \left( \frac{r_0}{r_{k0}} \right)^9 - \frac{1}{3} \left( \frac{r_0}{r_{k0}} \right)^3 \right] \bar{\mathbf{r}}_{k0}, \quad (27)$$

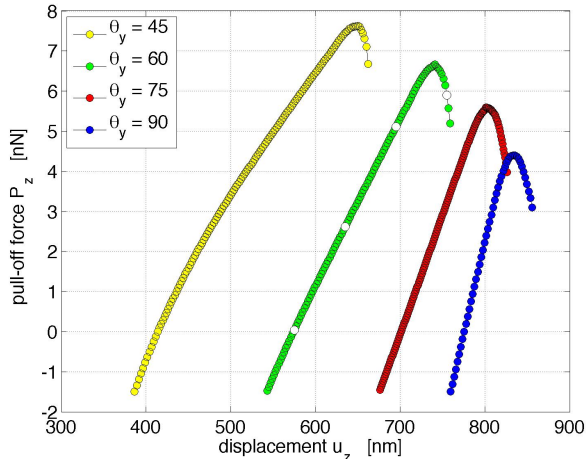


Figure 8: Spatula pull-off force  $P_z$  in dependence of  $u_z$  for various shaft inclination angles  $\theta_y$ . The white points for  $\theta_y = 60^\circ$  mark the four configurations shown in Fig. 7.

$\theta_y$	$P_{\max}$ [nN]	$\Delta u_z$ [nm]	$\Delta \Pi_{\text{ext}}$ [ $10^{-18} \text{ J}$ ]
$45^\circ$	7.63	248	1097
$60^\circ$	6.67	185	701
$75^\circ$	5.59	125	422
$90^\circ$	4.40	80	235

Table 6: Pull-off forces  $P_{\max}$ , pull-off displacements  $\Delta u_z$  (at detachment) and pull-off work  $\Delta \Pi_{\text{ext}}$  for different shaft inclinations  $\theta_y$ .

where  $r_{k0} = \sqrt{r_s^2 + r_a^2}$  denotes the overall distance surface point  $\mathbf{x}_1$  has moved in normal and tangential direction (contributions  $r_s$  and  $r_a$ ) and  $\bar{\mathbf{r}}_{k0}$  denotes the normalized direction along  $r_{k0}$ . As long as  $r_a = 0$ , contact laws (27) and (16) are equal. For  $r_a \neq 0$ , tangential contact forces are generated. The force separation law of these forces is the same as for the normal forces. This is similar to cohesive zone models with equal behavior in mode I and mode II separation. This implies that the separation energy is equal for both modes. Contact law (27), contrary to contact law (16), is unstable in compression (Sauer and Li, 2007). Therefore a penalty-type contact formulation, active only for compression, is included in the description. Fig. 9 shows the pull-off behavior of the spatula model for frictional contact according to eq. (27) compared to the frictionless result from Sec. 4.2. As seen, the friction forces hardly affects the peeling curve. At the beginning, the peeling forces are larger, but then later they become lower. The maximum pull-off force is now 6.45 nN instead of 6.67 nN. The small difference is perhaps not so surprising, since the considered vertical loading predominantly triggers mode I behavior, which is already captured in the original contact law (16). The fact that the maximum pull-off force has only decreased by 3.4% implies that tangential interface motions reduce the normal adhesion forces by a similar amount in contact law (27). The pull-off work  $\Delta \Pi_{\text{ext}}$  for both cases is  $0.70 \cdot 10^{-15} \text{ J}$ .

The friction study shows that frictional contact forces have a minor and negligible effect on peeling by vertical loading. Therefore, contact law (16) is considered for the remaining computations. The situation can be expected to change once a horizontal loading component is considered. In this case very large tangential contact forces may occur so that one needs to develop a sliding friction formulation for adhesive contact. This will be studied in future research.

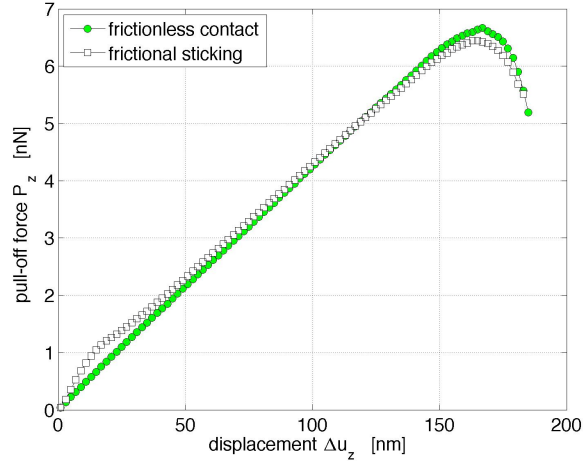


Figure 9: Spatula pull-off force  $P_z(\Delta u_z)$  for vertical peeling with frictional and frictionless contact. A shaft inclination angle of  $\theta_y = 60^\circ$  is considered.

#### 4.4 Spatula peeling force for various material parameters

Sec. 4.2 investigates the pull-off behavior of the spatula for different shaft inclinations. Now, the inclination is kept fixed at  $60^\circ$ , and different values for the material parameters  $\gamma_L$  are  $\gamma_W$ , defined in eq. (19), are considered. This study is useful to cover the uncertainties in the spatula stiffness, adhesion and size. Increasing  $\gamma_W$  by a factor of  $c$  corresponds to either increasing the spatula stiffness by the factor  $c$  or decreasing the adhesion forces by the factor  $c$ . Increasing  $\gamma_L$  by a factor of  $c$  corresponds to either increasing the spatula size by  $c$  or decreasing the range of adhesion by  $c$ . Here, the seven cases  $\gamma_W/\gamma_{W0} = 1.5^{-1}, 1, 1.5, 1.5^2$ , for fixed  $\gamma_L/\gamma_{L0} = 1$ , and  $\gamma_L/\gamma_{L0} = 1.5^{-2}, 1.5^{-1}, 1, 1.5$ , for fixed  $\gamma_W/\gamma_{W0} = 1$ , are considered. Their influence on the pull-off curves is shown in Fig. 10. The white points mark the maximum and zero force

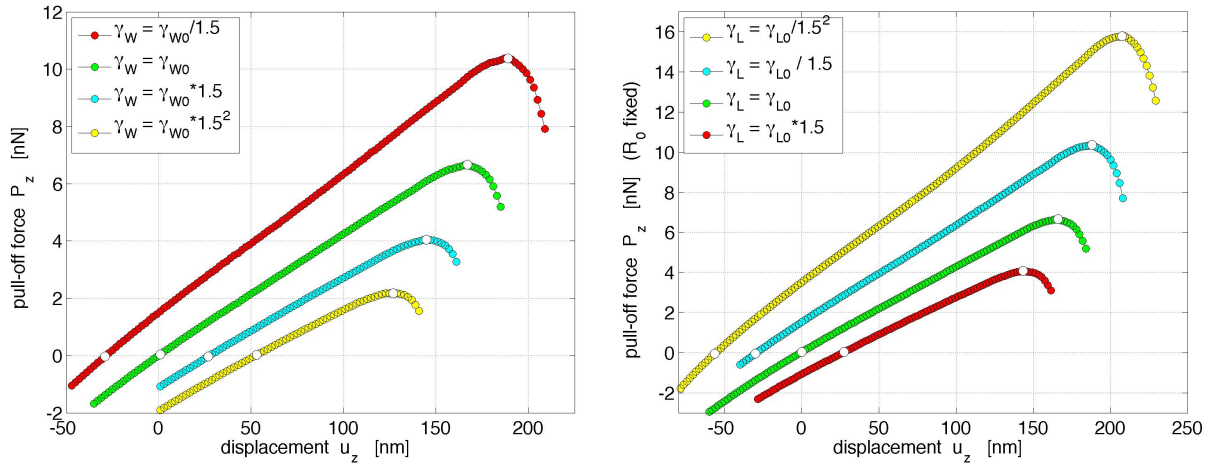


Figure 10: Load displacement curves for different adhesion parameters  $\gamma_W$  (left) and for different length scales  $\gamma_L$  (right) expressed as multiples of  $\gamma_{W0} = 25.266$  and  $\gamma_{L0} = 2.5$ . The shaft inclination is kept fixed at  $\theta_y = 60^\circ$ .

configurations shown in Figs. 11 and 12 below. As before, the coordinate  $\Delta u_z$  measures the  $z$ -

displacement of the center of the shaft end face from the completely undeformed configuration. The curves show that the pull-off force and energy increases for decreasing  $\gamma_W$  and  $\gamma_L$ . It is emphasized that this increase is not proportional to  $\gamma_W^{-1}$  or  $\gamma_L^{-1}$  due to the non-linearities of large deformations. It also seems that there is no combined parameter  $\gamma_C$ , that describes the influence of both  $\gamma_W$  or  $\gamma_L$ , as in the case for the adhesion of spheres (Sauer and Li, 2008). A detailed analysis of the seven different cases is given in Tabs. 7 and 8. The maximum pull-off

$\gamma_W/\gamma_{W0}$	$P_{\max}$ [nN]	$\Delta u_z$ [nm]	$\Delta \Pi_{\text{ext}}$ [ $10^{-18}$ J]
$1.5^{-1}$	10.38	238	1365
1	6.67	185	701
1.5	4.05	134	317
$1.5^2$	2.18	90	107

Table 7: Pull-off force, displacement and work for different adhesion parameters  $\gamma_W$ , considering  $\gamma_L = \gamma_{L0}$  and  $\theta_y = 60^\circ$

$\gamma_L/\gamma_{L0}$	$P_{\max}$ [nN]	$\Delta u_z$ [nm]	$\Delta \Pi_{\text{ext}}$ [ $10^{-18}$ J]
$1.5^{-2}$	15.78	285	2424
$1.5^{-1}$	10.36	237	1368
1	6.67	185	701
1.5	4.09	135	323

Table 8: Pull-off force, displacement and work for different adhesion parameters  $\gamma_L$ , considering  $\gamma_W = \gamma_{W0}$  and  $\theta_y = 60^\circ$ .

forces lie in the range between 2 nN and 16 nN, which agrees well with the range observed by Huber et al. (2005) and Sun et al. (2005). The pull-off energy (per spatula) lies in the range of  $0.1 \cdot 10^{-15}$  J to  $2.5 \cdot 10^{-15}$  J.

Fig. 11 compares the spatula deformation and stress at  $P_z = 0$  and  $P_z = P_{\max}$  for the four considered adhesion parameters  $\gamma_W/\gamma_{W0} = 1.5^{-1}, 1, 1.5, 1.5^2$ . As can be expected, the deformation and stress increase as the strength of adhesion increases (for decreasing  $\gamma_W$ ). In particular, the pad area adhering to the substrate for  $P_z = 0$ , increases. Note that decreasing  $\gamma_W$  can also be viewed as decreasing the material stiffness. The maximum peeling stress at the underside of the pad, which is given by eq. (22), is proportional to  $\gamma_W^{-1}$ . However, this proportionality does not extend to  $P_{\max}$ ,  $\Delta u_z$  and  $\Delta \Pi_{\text{ext}}$ , as is seen from Tab. 7. It becomes clear from these results, that the spatula will not function anymore if the adhesion is too weak or the material too stiff. In the present example (shaft inclination of  $60^\circ$ ), the case  $\gamma_W = 1.5^2 \gamma_{W0}$  is probably already too weak to represent a useful spatula design. On the other hand, strong adhesion produces very large stresses and strains in the spatula structure, which may eventually cause the rupture of the structure. In current research, failure mechanisms of the spatula, and also the gecko seta, remain open topics.

Analogously to Fig. 11, Fig. 12 shows the spatula deformation and stress at  $P_z = 0$  and  $P_z = P_{\max}$  for the four considered length scales  $\gamma_L/\gamma_{L0} = 1.5^{-2}, 1.5^{-1}, 1, 1.5$ . Here, the geometry is normalized by  $R_0$ , so that the four different spatulae appear equally large. The actual relative sizes differ substantially. In this case, the deformation and stress increases for decreasing spatula size (decreasing  $\gamma_L$ ). Then, also the relative pad area adhering to the substrate for  $P_z = 0$ , increases. Note that decreasing  $\gamma_L$  can also be viewed as increasing the range of adhesion  $r_0$ . The maximum peeling stress at the underside of the pad (see eq. (22)), is also proportional to  $\gamma_L^{-1}$ . But again, this proportionality does not extend to  $P_{\max}$ ,  $\Delta u_z$  and  $\Delta \Pi_{\text{ext}}$ , as is seen

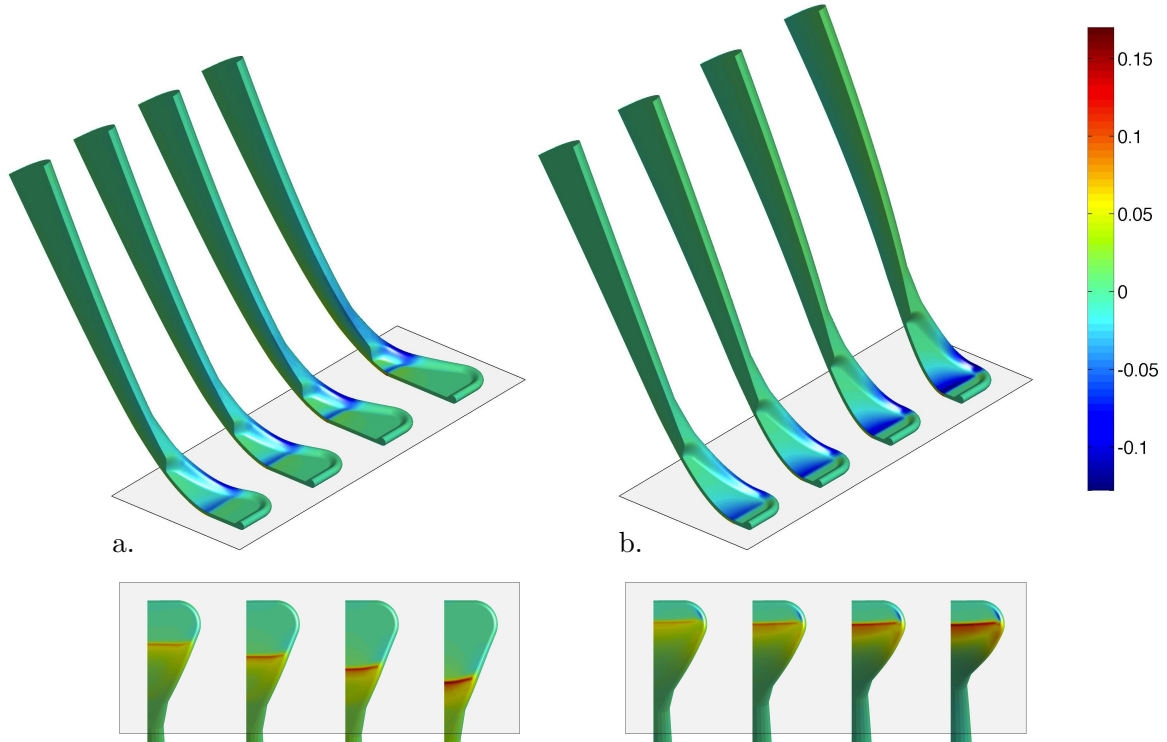


Figure 11: Spatula deformation for various  $\gamma_W$ : a. initial, pre-rotated configuration ( $P_z = 0$ ); b. deformation at maximum peeling force ( $P_z = P_{\max}$ ). In both (a) and (b),  $\gamma_W$  decreases from left to right. The lower images show the bottom view of the spatula pad. The colorscale shows  $I_1 = \text{tr } \boldsymbol{\sigma}$ , normalized by  $E$ .

from Tab. 8. If the size of the spatula becomes too large, it will lose its functionality due to its increased stiffness. Too small spatula sizes, on the other lead to large stresses and strains.

#### 4.5 Spatula adhesion to a rough substrate

The results presented so far consider a perfectly smooth substrate surface. Realistically, this surface will be characterized by some form of roughness. The detailedness of the presented spatula model is ideal to investigate the influence of this roughness on the adhesion properties of the spatula. As a numerical example, which demonstrates the remarkable adhesion strength of the spatula, we consider the adhesion of the spatula pad to an idealized, rough surface. The roughness of this surface is constructed as a superposition of single asperities that are described by the exponential function

$$z(x, y) = z_0 \exp\left(-\frac{x^2 + y^2}{h^2}\right). \quad (28)$$

Here the parameter  $h$  is a length scale that describes the sharpness of the asperity: large  $h$  characterize relatively flat waves, whereas small  $h$  characterize relatively sharp spikes. The asperities are considered to have equal height  $z_0$  and are arranged in a triangular grid as is shown in Fig. 13. This surface can be quite easily incorporated into the contact algorithm of the considered adhesion model (Sauer and Wriggers, 2009). A closest point projection has to be carried out for every surface point of the spatula pad, in order to obtain the distance and direction of the neighboring substrate, which are needed for eq. (16).

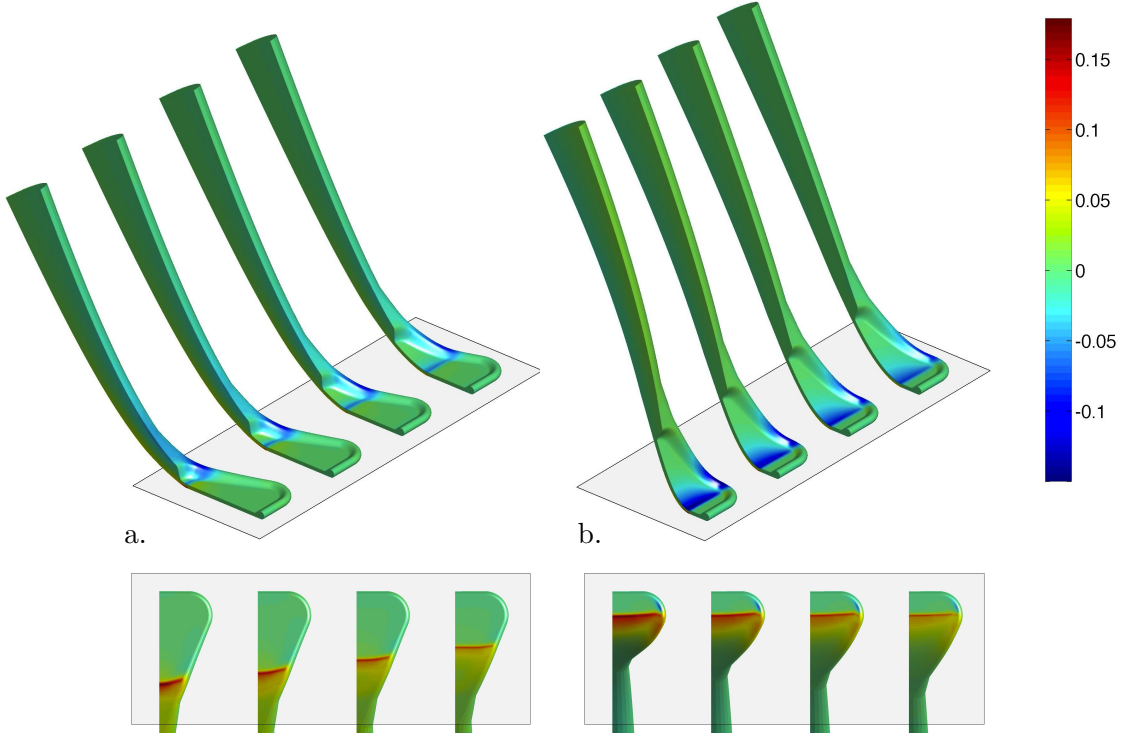


Figure 12: Spatula deformation for various  $\gamma_L$ : a. initial, pre-rotated configuration ( $P_z = 0$ ); b. deformation at maximum peeling force ( $P_z = P_{\max}$ ). In both (a) and (b),  $\gamma_L$  increases from left to right. The lower images show the bottom view of the spatula pad. The colorscale shows  $I_1 = \text{tr } \boldsymbol{\sigma}$  normalized by  $E$ .

Fig. 14 shows the contact deformation and stresses for a spatula adhering to the surface shown in Fig. 13. Three different roughness levels,  $z_0 = 0$ ,  $z_0 = 4$  nm and  $z_0 = 8$  nm, are considered. For each, sharpness parameter  $h$  is set to  $h = 20$  nm and the distance between neighboring asperities is taken as  $\lambda = 100$  nm. In all cases the inclination of the spatula shaft is kept fixed at  $\theta_y = 45^\circ$  and the net force acting on the end face is taken as zero. The figure shows that, even for  $z_0 = 8$  nm, most of the pad is still fully adhering to the rough substrate. The contact surface is the area enclosed by the peeling zone, which appears as a red band in the stress plot. This means that the spatula is sufficiently compliant to adapt to the substrate roughness, which is quite remarkable. The stresses caused by the pad deformation exceed by far the stress level of the pull-off computations seen in the previous sections. This indicates that the spatula stress is determined predominantly by the roughness of the substrate. The surface roughness also has a strong influence on the numerical computations. During peeling of the pad, the peeling zone advances across the asperities, which can cause local instabilities in the system. Advanced contact algorithms need to be developed to handle such instabilities.

## 5 Conclusion

This paper presents a detailed three dimensional, parametric geometry model for a gecko spatula and uses this model to study the peeling behavior of the spatula for various model parameters and loading conditions. The mechanical formulation is based on the 3D, finite element based, computational adhesion formulation of Sauer and Wriggers (2009), which is outlined in Sec. 3.

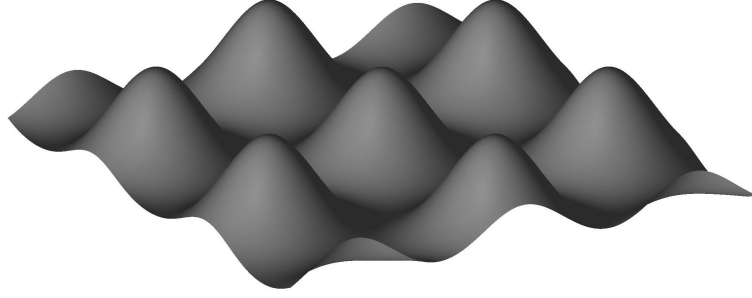


Figure 13: Rough surface model based on eq. (28) considering a periodic triangular grid of asperities with distance  $\lambda$ .

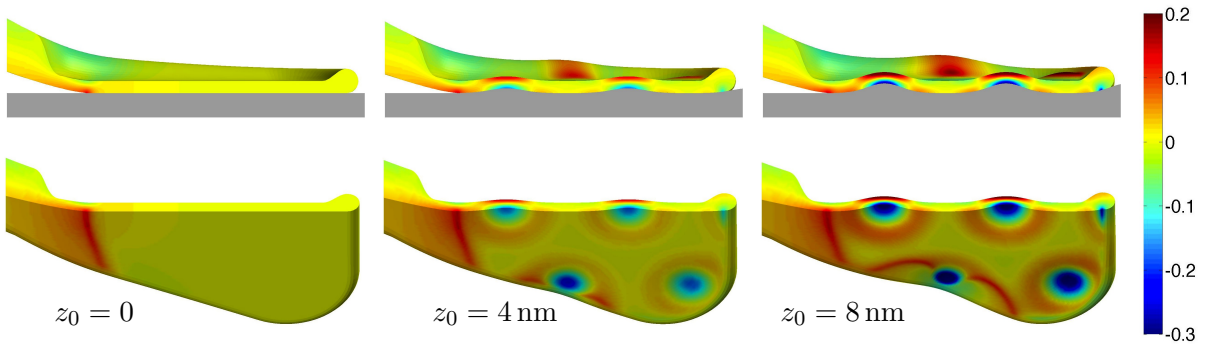


Figure 14: Spatula adhesion to a rough surface for various asperity heights  $z_0$ . The top row shows the side view of the pad and the rough substrate. The bottom row shows the bottom view of the pad. The area enclosed by the peeling front is fully in contact. The truncated colorscale shows  $I_1/E$ , which lies between -0.415 and 0.294.

Among the different cases that are studied here, are the influences of variations in spatula size, spatula stiffness, strength of adhesion, range of adhesion, surface roughness, stiction and loading conditions.

The proposed spatula model offers several advantages over previously considered spatula models. The first is that the geometry description is parameterized, which allows to easily consider size and shape changes, and conduct geometry optimization studies. Here, the effect of different spatula sizes has been investigated. A study of different shapes will be considered in the future. A second advantage of the proposed spatula model is the detailed 3D analysis it allows. The stress and strain fields can be analyzed and large stress concentrations can then be used to define criteria for shape optimization and material failure. A third advantage is the possibility to study the contact on rough substrate surfaces and to determine its influence on the effective spatula performance.

Even though the gecko spatula is very small – the pad is only about 10 nanometers thick – it is still so large that a very high number of finite elements is required in order to model van der Waals adhesion between the spatula pad and a substrate robustly. A highly efficient contact enrichment technique has been developed for this purpose in Sauer (2011a). This technique is used here since it allows the use of a moderately coarse finite element discretization, where the contact surface elements are no smaller than 2.87 nm in diameter.

The numerical studies conducted here, allow us to draw several conclusions: First of all, the pull-off forces obtained from the proposed model fall into the experimental range reported in

the literature. Secondly, the study shows that the gecko spatula can function over a wide range of model parameters. In the extreme cases the spatula either loses its adhesive property or it will exhibit very large stresses. Finally, the rough surface computations show that the spatula adhesion is so strong that there can be intimate contact between spatula pad and substrate even for very rough surfaces. The effect of rough surfaces is a topic that needs to be investigated in further detail in the future. Another important extension is the consideration of tangential loading components. Since these can cause very large tangential contact forces, the formulation of accurate sticking and sliding friction models for adhesive contact is necessary. There are also several other future applications that can be studied with the present model. One is the development of multiscale models that describe entire gecko setae. In this regard it is also helpful to develop reduced order models, that capture the effective spatula behavior. The present model can then be used as a reference model. Another future application are shape optimization studies. For these purposes it is also useful to refine the model, for example by considering inertia, friction or by considering dissipative material response.

## Acknowledgements

The authors are grateful to the German Research Foundation (DFG) for supporting this research under project SA1822/5-1 and grant GSC 111. The authors also wish to thank the Institute of Continuum Mechanics for its initial support of this work.

## A Detailed description of the modeled spatula geometry

This section describes the four parts used to model the gecko spatula. For illustration, the reader is referred to Figs. 2 and 3. The interface surfaces between the four parts are perpendicular to the  $\{X, Y\}$ -plane (i.e. the surface normals of all interfaces are parallel to the  $\{X, Y\}$ -plane). The parts can therefore be uniquely defined in the  $\{X, Y\}$ -representation shown in Fig. 2.

Part  $\mathcal{P}_I$  consists of the shaft and the outer rim of the pad. It is formed by a curved cylinder whose axis follows the curve through points  $\{P_1, P_2, \dots, P_7\}$ . The cylinder has an elliptical cross-section. The first half width of the ellipse is aligned with the  $Z$ -axis and is denoted  $a$ , the second half width is aligned with the  $\{X, Y\}$ -plane and is denoted  $b$ . Between points  $P_1$  and  $P_2$ , the two half widths  $a$  and  $b$  vary linearly between  $c_s$  and  $a_s$ , and between  $c_s$  and  $b_s$ . Between point  $P_2$  and point  $P_7$ , the half width  $a$  is equal to the  $Z$  coordinate of the dashed curve between  $P_2$  and  $P_7$ , which is described by a circle in the  $\{X, Z\}$ -plane with radius  $r_5$  and center at  $P_{15}$ . Half width  $b$  is set equal to  $a$  for the stretch between  $P_3$  and  $P_7$ . From  $P_2$  to  $P_3$ ,  $b$  varies linearly between  $b_s$  and  $a(P_3)$ . The elliptical cross-section of  $\mathcal{P}_I$  is oriented such that  $a$  is parallel to the  $Z$ -axis while  $b$ , at  $P_1$  and along  $\{P_3, \dots, P_7\}$ , is parallel to the  $\{X, Y\}$ -plane and perpendicular to the cylinder axis. At  $P_2$ , the axis has a kink and the half axis  $b$  is aligned with the bisector of the kink angle. Along the axis between points  $P_1$  and  $P_3$  the direction of the half width is found by the linear interpolation of the directions at  $P_1$ ,  $P_2$  and  $P_3$ . Between points  $P_1$  and  $P_2$ , the shaft is inclined by  $\theta_s$ .

Part  $\mathcal{P}_{II}$  is the region enclosed by the curve through points  $\{P_{12}, P_3, P_4, \dots, P_{12}\}$ . The  $Z$ -height of  $\mathcal{P}_{II}$  is equal to the  $Z$ -height of  $\mathcal{P}_I$  along their common interface surface (through points  $\{P_3, P_4, \dots, P_7\}$ ) and reduces down to the pad thickness  $h_p$  at the inner boundary (through points  $\{P_8, P_9, \dots, P_{11}\}$ ). In the region  $\{P_{12}, P_4, \dots, P_{12}\}$  the height is varied using a cosine function such that the slope of the top surface across the interface  $\{P_{12}, P_4, \dots, P_{12}\}$  is continuous. Along  $\{P_4, \dots, P_{12}\}$  this slope is horizontal (i.e. parallel to the  $\{X, Y\}$ -plane). Along  $\{P_{12}, P_4\}$  the slope is not horizontal as it is adapted to the slope of the top height of the rim, which follows from parameters  $r_5$  (defining line  $P_3$  to  $P_4$ ) and  $a$ . The top surface of the corner region

$\{P_3, P_4, P_{12}, P_3\}$  is also equal to the top height of the rim. This produces a smooth transition at the junction of regions  $\mathcal{P}_I$ ,  $\mathcal{P}_{II}$  and  $\mathcal{P}_{III}$ .

Part  $\mathcal{P}_{III}$  is formed by the triangular prism bounded by the interface through points  $\{P_2, P_3, P_{12}\}$ . The  $Z$ -height is equal to  $2a$ .

Part  $\mathcal{P}_{IV}$  has constant  $Z$ -height  $h_p$  and is bounded by the interface through points  $\{P_8, P_9, P_{10}, P_{11}, P_8\}$ .

## References

- Arzt, E., Gorb, S., and Spolenak, R. (2003). From micro to nano contacts in biological attachment devices. *Proc. Natl. Acad. Sci. USA*, **100**(19):10603–10606.
- Autumn, K., Dittmore, A., Santos, D., Spenko, M., and Cutkosky, M. (2006). Frictional adhesion: a new angle on gecko attachment. *J. Exp. Biol.*, **209**:3569–3579.
- Autumn, K., Liang, Y. A., Hsieh, S. T., Zesch, W., Chan, W. P., Kenny, T. W., Fearing, R., and Full, R. J. (2000). Adhesive force of a single gecko foot-hair. *Nature*, **405**:681–684.
- Huber, G., Mantz, H., Spolenak, R., Mecke, K., Jacobs, K., Gorb, S. N., and Arzt, E. (2005). Evidence for capillarity contributions to gecko adhesion from single spatula nanomechanical measurements. *Proc. Natl. Acad. Sci. USA*, **102**(45):16293–16296.
- Israelachvili, J. N. (1991). *Intermolecular and Surface Forces*. Academic Press, 2<sup>nd</sup> edition.
- Johnson, K. L., Kendall, K., and Roberts, A. D. (1971). Surface energy and the contact of elastic solids. *Proc. R. Soc. Lond. A*, **324**:301–313.
- Kendall, K. (1975). Thin-film peeling – the elastic term. *J. Phys. D: Appl. Phys.*, **8**:1449–1452.
- Kwaki, J. S. and Kim, T. W. (2010). A review of adhesion and friction models for gecko feet. *Int. J. Precis. Eng. Manuf.*, **11**(1):171–186.
- Rizzo, N. W., Gardner, K. H., Walls, D. J., Keiper-Hrynko, N. M., Ganzke, T. S., and Hallahan, D. L. (2006). Characterization of the structure and composition of gecko adhesive setae. *J. R. Soc. Interface*, **3**:441–451.
- Sauer, R. A. (2009). Multiscale modeling and simulation of the deformation and adhesion of a single gecko seta. *Comp. Meth. Biomech. Biomed. Engng.*, **12**(6):627–640.
- Sauer, R. A. (2010). A computational model for nanoscale adhesion between deformable solids and its application to gecko adhesion. *J. Adhes. Sci. Technol.*, **24**:1807–1818.
- Sauer, R. A. (2011a). Enriched contact finite elements for stable peeling computations. *Int. J. Numer. Meth. Engrg.*, **87**:593–616.
- Sauer, R. A. (2011b). The peeling behavior of thin films with finite bending stiffness and the implications on gecko adhesion. *J. Adhes.*, **87**(7-8):624–643.
- Sauer, R. A. (2012a). Computational contact formulations for soft body adhesion. In Li, S. and Sun, B., editors, *Advances in Soft Matter Mechanics*. Springer.
- Sauer, R. A. (2012b). A geometrically exact finite beam element formulation for thin film peeling. *in preparation*.

- Sauer, R. A. and Li, S. (2007). A contact mechanics model for quasi-continua. *Int. J. Numer. Meth. Engrg.*, **71**(8):931–962.
- Sauer, R. A. and Li, S. (2008). An atomistically enriched continuum model for nanoscale contact mechanics and its application to contact scaling. *J. Nanosci. Nanotech.*, **8**(7):3757–3773.
- Sauer, R. A. and Wriggers, P. (2009). Formulation and analysis of a 3D finite element implementation for adhesive contact at the nanoscale. *Comput. Methods Appl. Mech. Engrg.*, **198**:3871–3883.
- Sun, W., Neuzil, P., Kustandi, T. S., Oh, S., and Samper, D. (2005). The nature of the gecko lizard adhesive force. *Biophys. J.*, **89**(2):L14–L17.
- Tian, Y., Pesika, N., Zeng, H., Rosenberg, K., Zhao, B., McGuiggan, P., Autumn, K., and Israelachvili, J. (2006). Adhesion and friction in gecko toe attachment and detachment. *Proc. Natl. Acad. Sci. USA*, **103**(51):19320–19325.
- Wriggers, P. and Reinelt, J. (2009). Multi-scale approach for frictional contact of elastomers on rough rigid surfaces. *Comput. Methods Appl. Mech. Engrg.*, **198**(21-26):1996–2008.
- Xu, X.-P. and Needleman, A. (1993). Void nucleation by inclusion debonding in a crystal matrix. *Model. Simul. Mater. Sci. Engng.*, **1**(2):111–132.